SAND2013-6575C

VALIDATION OF ALEGRA-MHD TO MODEL CONFINED ELECTRICAL DISCHARGES

Thomas A. Haill[1,a], Kenneth M. Williamson[1,b], Raymond Martinez[2], and Jane M. Lehr[1]

[1]Sandia National Laboratories, Albuquerque, NM, USA
[2]Science Applications International Corporation, Albuquerque, NM, USA
[a]tahaill@sandia.gov, [b]kwilli1@sandia.gov

ABSTRACT

Sandia National Laboratories is developing the capability to predict thermal and electrical characteristics of short arcs that may appear in equipment subjected to transient currents of hundreds or thousands of amperes. This capability is critical to assuring functionality and protection of sensitive equipment in extreme environments. Penetration of electrical energy can impact sealed metallic compound joints through delamination, spalling, and burn through. Herein, the focus is on predicting structural integrity of compound joints subjected to lightning strikes. Joint-materials respond to multiple physical phenomenon including thermal energy, shock waves, and changes of state that result from axial confinement of lightning-induced electrical discharge. This paper presents models and simulations of the late-time expansion phase of arcing that result from lightning-like currents (with peaks of 1 kA to 10 kA and an 8 μs rise time). Simulations were performed using ALEGRA-MHD and incorporated Lagrangian tracers in the dielectric and electrode surfaces recording simulated particle velocities and displacements, pressure pulses, density, and temperature changes. Experimental results from axially confined exploding wires in an air gap, confined exploding wires in potted materials, and finally arc breakdown through and shock generation in potted materials are compared to the ALEGRA models. Comparisons include measured voltages, currents, and radially expanding shock waves captured by time-gated Schlieren images.

INTRODUCTION

To understand and quantify the behavior of confined arcs, two-dimensional, axially-symmetric numerical simulations of the electrical breakdown experiments were performed with the ALEGRA-MHD code [1-3]. ALEGRA-MHD is an Arbitrary-Lagrangian-Eulerian (ALE) finite-element code that models dynamic mechanical response and shock propagation in a resistive magneto-hydrodynamic environment. The code includes thermal conduction and is coupled to state of the art material models. The code also includes radiation physics if needed.

The 2D ALEGRA-MHD simulations of the electrical breakdown experiments model two 25-mm diameter electrodes with a thin wire and a gap material in between, as well as a portion of the ambient air which surrounds the experiment. The simulations are driven by a Thevenin equivalent circuit model of the waveform generator and experimental apparatus. Lagrangian tracers located in the gap material and in the surfaces of the electrodes record the simulated particle velocities and displacements, pressure pulses, and density and temperature changes.

EXPERIMENTAL APPROACH TO ELECTRICAL BREAKDOWN EXPERIMENTS

The experimental configuration consists of two metallic plates (1-inch diameter electrodes) placed parallel to each other and separated by a small distance as shown in Figures 1 and 2. The top plate is driven with an electrical pulse of current representative of a lightning waveform. The bottom plate is grounded and a non-conducting material is placed between the plates. The plates act as boundaries that limit the volume between the plates. A thin aluminum wire is placed between the center of the top plate and center of the bottom plate to act as an initiator wire for the arc as shown in Figure 2. This ensures the arc's path between the electrodes. The wire radius is chosen such that the current source can explode the wire.

The excitation pulse is provided by commercially available surge generators which provide the waveforms required by industry standards for surge/voltage testing in both open and short circuits. Two such generators have been employed, the first a Velonex model 590 generator capable of surge currents up to 4.5 kA, and the second a HILO model PG 24-2500 generator capable of surge currents up to 12 kA and surge voltages of 25 kV. The circuitry is solid state and the units come with internal voltage and current monitors.

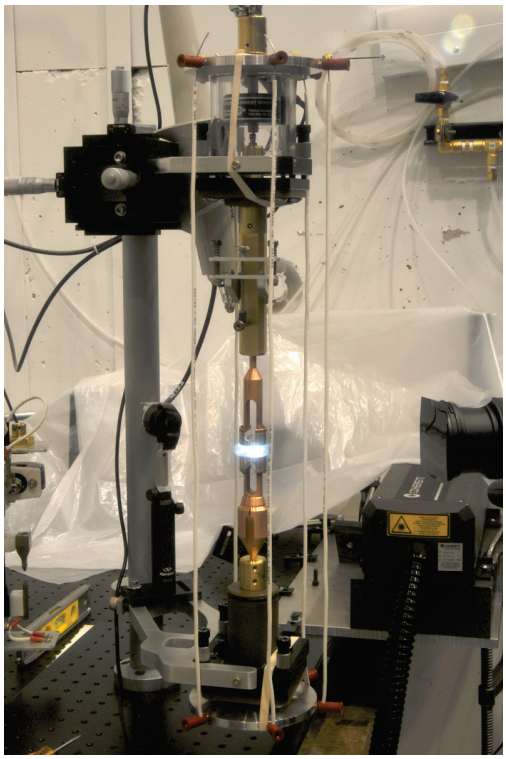

Figure 1. Photograph of the experimental fixture showing the self-emission from the breakdown of an aluminum wire in a 10 mm gap.

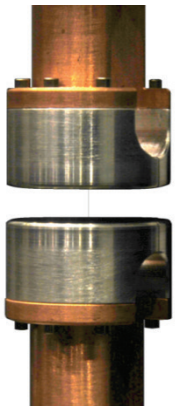

Figure 2. Close photograph of the anode and cathode pair. A thin 96.4 micron wire is barely visible in the 5 mm air gap.

An appropriate waveform for the current driver has a rise-time between 1 and 10 μs, a decay time of less than 50 μs and peak amplitude of up to 10 kA. The applied current is measured with a commercial current viewing transformer (CVT), a Pearson Model 411, which is calibrated in-house to traceable standards. The CVT measures the magnetic field associated with the time varying current without adding current-limiting resistance into the circuit.

The voltage drop across the exploding wire is measured with a high voltage probe (Tektronix P6015A) capable of measuring voltages to 20 kV DC and even higher pulsed voltages. The Tek6015 is a high impedance (100 MΩ, 3 pF) passive voltage divider with a 75 MHz bandwidth. The voltage signal is measured at the CVT411 position and referenced to ground by attaching an alligator clip lead to the grounded fixture.

For large enough (>0.5mm) inter-electrode gaps and for transparent gap materials, the wire explosion and shock propagation in the gap material are recorded using a laser Schlieren imaging diagnostic coupled to a gated Andor ICCD camera. The Andor ICCD camera is set with a 5 ns gate length. A variable set of delay times is adjusted over a series of shots with the same parameters to construct a sequence of pictures of the evolution of the shock wave. Several Schlieren images are shown later in this report.

Experiments to obtain data to validate the code have been conducted. In particular, quantities must be measured which can also be calculated, such as pressure as a function of radius and time, as well as other quantities that can be calculated. In practice, what is feasible to be measured drives the quantity that will be compared. Quantities of interest are temperature, density, and pressure versus radius, position, and time.

MHD SIMULATIONS APPROACH TO THE ELECTRICAL BREAKDOWN EXPERIMENTS

General Simulation Setup

All wire burst simulations discussed in this report are 2D cylindrically symmetric simulations that model the wire and the surfaces of the upper and lower electrodes. The general simulation geometry is shown in Figure 3. The wire is located on axis and extends the full height of the mesh. Most wire diameters are 96.4 microns. The upper and lower electrodes are 1 inch (25.4 mm) in diameter with a 31 mil (0.79 mm) radius of curvature at the corner. Only the first 80 mils (2.03 mm) of the electrode surface is modeled in height. The overall geometry height depends upon the height of the wire and gap between the electrodes.

The mesh is rectilinear and Eulerian. Mesh resolution in the wire is 2 microns radially and 5 microns axially for longer wires and 2 microns for short wires (less than 1 mm). This radial resolution extends to 4 times the wire radius. Outside this radius the mesh cell size is graded radially up to

4 mils (0.102 mm) at the outer radius of the electrode and also graded axially to the same size at the top and bottom of the mesh.

All materials are initialized to 1 atmosphere pressure. Even though the wire and the electrodes are both aluminum, they are of two types. Wires are cut from spools of Al 5056, while the electrodes are machined from Al 6061-T6. The two materials are given different material identification numbers to distinguish them in the simulations.

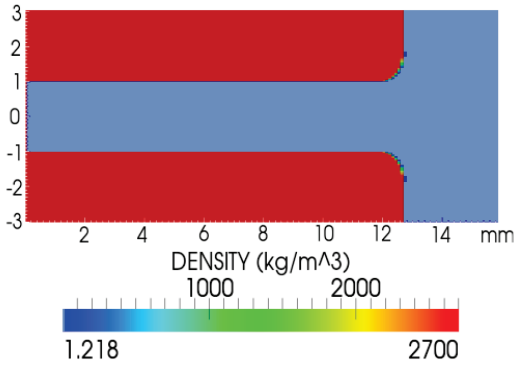

Figure 3. General wire burst geometry showing wire on axis and 2 mm of the axial height of the 1 inch diameter electrodes. Air fills the gap and surrounds the electrodes. In some experiments and simulations various other materials fill the gap.

Hydrodynamic boundary conditions include a no displacement boundary condition on axis, while the top, bottom and outer radius have a 1 atmosphere pressure boundary condition applied. Specifying a constant pressure boundary condition prevents artificial expansion of materials off of the mesh, but allows pressures waves to be transmitted through the boundary and into virtual material surrounding the computational domain. Thermal conduction boundary conditions specify no heat flux through all boundaries. Magnetic boundary conditions have zero magnetic field on axis and the current density is normal to the top and bottom boundaries (zero normal magnetic field). A time-dependent azimuthal magnetic field is applied to the outer radial boundary and is proportional to the total current flowing in the conductors as specified by Ampere's Law.

$$B_\theta(R,t) = \frac{\mu_0 I(t)}{2\pi R} \qquad (1)$$

The current as a function of time may be specified by an experimentally measured current waveform that is coupled to the mesh by directly driving the magnetic boundary condition through Equation 1 using a simple circuit coupling as in Figure 4. The advantage of this method over directly driving the boundary condition is that the voltage between the two nodes (black dots of the figure) will inform the user of the voltage across the simulation domain. However, the simulation voltages driven in this manner are always several times higher than the experimental voltages. This is due to the fact that the method will force the prescribed current to flow through the simulation domain whether the state of the material is reasonably able to accept the current or not. There is no mechanism for the simulation to provide feedback to the driving current.

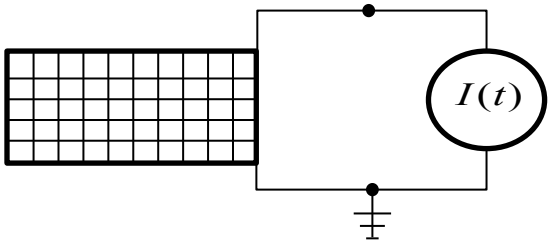

Figure 4. Simple source current equivalent circuit model to drive wire burst simulations.

Alternatively, the current may be computed by an equivalent circuit model representing the pulser as in Figure 6. The development of an equivalent circuit model is the subject of the next subsection.

Development of a Thevenin Equivilent Circuit Model to Represent the Pulser Source

The ultimate goal of the modeling and simulation effort is to develop a predictive capability for modeling wire burst when the wire is confined between a pair of electrodes and also surrounded by various materials located in the gap between the electrodes. In some experiments the gap material is opaque, and in other experiments the gap is small enough, so that the burst of the wire cannot be clearly imaged. Only the late time shock as the shock exits the gap material possibly is imaged. This leaves only the electrical signals as the main diagnostic of wire burst. Therefore, while electrical waveforms measured at the wire load can be used to drive simulations, they cannot be used in a predictive manner. This section develops the equivalent circuit model to drive simulations in the quest of a truly predictive modeling capability.

The equivalent circuit model must be developed empirically. The circuit model should reflect the

various components used in the experiments, as well as the diagnostics used to measure the voltage and current. These components include:

- Velonex or HiLo pulser
- Coax cable connecting the pulser to the experiment
- Fixture to hold the wire
- Exploding wire load
- Voltage probe to measure voltage at the pulser
- Tektronix P6015A high voltage probe to measure voltage at the load
- Pearson Model 411 CVT current probe to measure current at the load

The basic building block of the equivalent circuit is the resistor-inductor-capacitor (RLC) circuit so we review the solution to that simple circuit.

Analytic Solution to Simple RLC Circuit Equations

The solution to a simple RLC circuit is found by starting with Kirchoff's voltage law which states that the sum of the voltages around a closed loop of a circuit is zero.

$$\begin{aligned} V_C - V_L - V_R &= 0 \\ \frac{q}{C} - L\dot{I} - RI &= 0 \end{aligned} \qquad (2)$$

As the charge q on the capacitor drops, the current in the circuit rises, thus $\dot{q} = -I$. Differentiating, substituting and rearranging leads to the following ordinary differential equation for the current.

$$\ddot{I} + \frac{R}{L}\dot{I} + \frac{1}{LC}I = 0 \qquad (3)$$

The initial boundary conditions are $I_0 = 0$ and $\dot{I}_0 = V_0/L$, where V_0 is the initial voltage on the capacitor. As can be found in many textbooks, the solution has 3 cases.

Case 1: Under-damped, Oscillatory Solution

The under-damped, oscillatory solution is:

$$I(t) = \frac{V_0}{\omega_0 L} \cdot \sin(\omega_0 t) \cdot \exp\left(-\frac{t}{\tau}\right) \qquad (4)$$

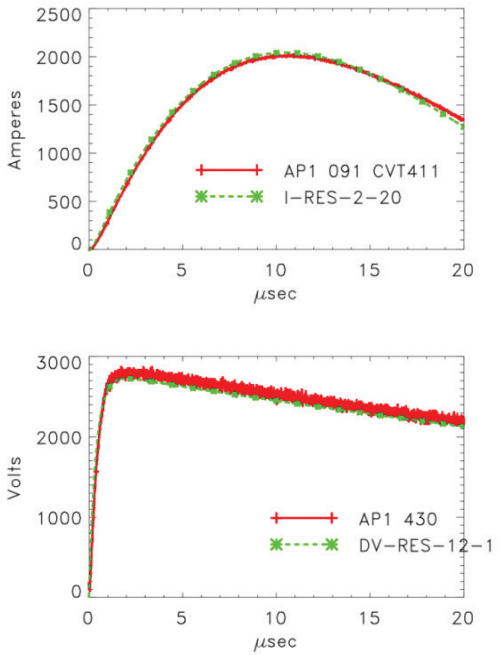

Figure 5. Comparisons of pulse generator circuit model to short circuit (top) and open circuit (bottom)

where $\omega_0 = \sqrt{\left(\frac{1}{LC}\right) - \left(\frac{R}{2L}\right)^2}$ and $\tau = \frac{2L}{R}$.

This solution exhibits both positive and negative current flow as the circuit energy oscillates back and forth between the capacitor and inductor (trigonometric sine function). Eventually, the energy is dissipated by the resistor (exponential term). Short circuit characterization shots driven by the current waveform generator are matched to this case. This case also represents the dominant behavior of the wire burst experiments. One example of a portion of the first half-cycle for this type of solution is shown in the top of Figure 5.

Case 2: Critically damped Solution

The critically damped solution is:

$$I(t) = \frac{V_0}{L} \cdot t \cdot \exp\left(-\frac{t}{\tau}\right) \qquad (5)$$

where $\omega_0 = 0$ and $\tau = \frac{2L}{R}$.

This solution is a special case and has not been seen in any of the current waveforms measured and examined.

Table 1.Summary of RLC circuit model parameters.

Shot number	Shot type	Velonex Dial setting	Voltage [V]	Capacitance [μF]	Inductance [μH]	Resistance [Ω]
AP1 001	open	1	1010	9.0	5.0	8.0
AP1 008	open	1	950	9.0	5.0	8.0
AP1 430	open	3	2789	9.0	3.0	8.0
AP2 005	open	3	2789	9.0	3.0	8.0
AP1 078	short	1	1500	12.6	5.0	8.0
AP1 091	short	3	3000	12.6	3.0	8.0
AP1 092	short	3	2250	12.6	3.0	8.0
Coax	Tline			0.383 nF	1.606 μH	47.6 mΩ

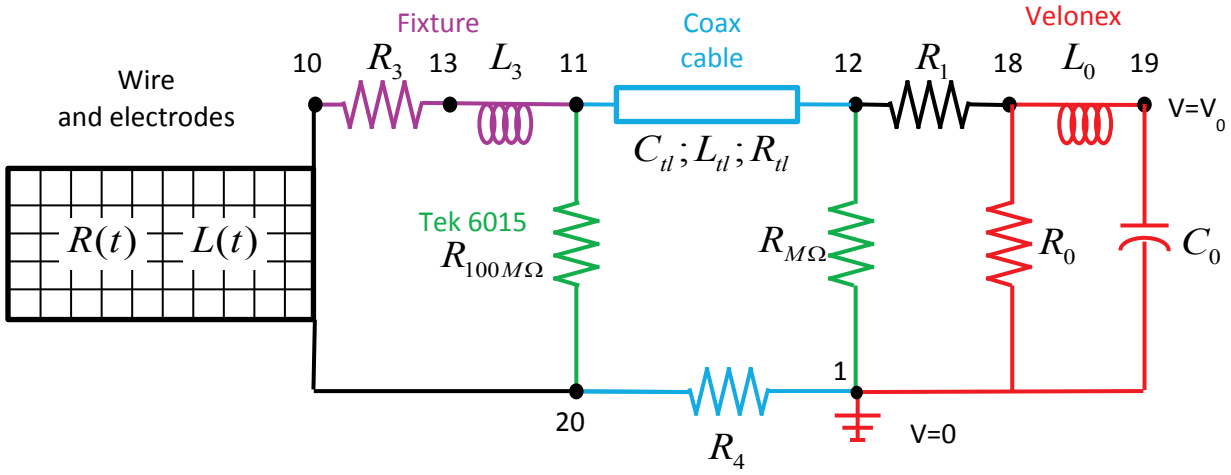

Figure 6. Thevenin equivalent circuit model of the pulse generator used to drive wire burst simulations.

Case 3: Over-damped Solution

The over-damped solution is:

$$I(t) = \frac{V_0}{\omega_0 L} \cdot \sinh\left(\omega_0 t\right) \cdot \exp\left(-\frac{t}{\tau}\right) \qquad (6)$$

where $\omega_0 = \sqrt{\left(\frac{R}{2L}\right)^2 - \left(\frac{1}{LC}\right)}$ and $\tau = \frac{2L}{R}$.

This solution exhibits only positive current and energy flows from the capacitor to the inductor, and eventually to the resistor where it is dissipated. The hyperbolic sine function diverges to infinity for late times, however brief analysis shows that the exponential decay term will dominate at late times, so the solution remains bounded. Open circuit characterization shots driven by the waveform generator, where no current flows to the wire load, but instead is dissipated in the pulser, is matched to this case. One example for this type of solution is shown in the bottom of Figure 5.

Complete Equivalent Circuit Model and Coupling to the Experimental Apparatus

Figure 6 summarizes the equivalent circuit model for the pulse generator, the coax cable, wire fixture, and wire load. The pulse generator is represented by the circuit elements C_0, L_0 and R_0. Values for these parameters are given by the open circuit values in Table 1. This portion of the circuit is over-damped.

The 14-ft (4.572 m) coax cable is represented by the transmission line element described by the total capacitance C_{tl}, inductance L_{tl} and resistance R_{tl}. Values for these parameters are also given in Table 1. The delay time is the time duration over which a voltage pulse will traverse the length of the cable. The formula for the delay time is:

$$\tau = \frac{d}{v} = \sqrt{L \cdot C} \qquad (7)$$

where d is the length of the coax cable and L and C are the total cable inductance and capacitance. The 24 ns delay time is fairly insignificant to the microsecond timescales of the experiments.

The resistor R_4 represents the outer braided conductor of the coax cable. The inductor L_3 and the resistor R_3 represent the wire holder fixture. Values for these parameters are given by the short circuit values in Table 1.

Figure 6 shows two other resistors $R_{M\Omega}$ and $R_{100M\Omega}$. These resistors represent the voltage dividers that measure the circuit voltage at the output of the pulse generator and at the load. Due to the large resistances of these circuit elements negligible current flows through them. The pulse generator has outputs that are connected to a 1 MΩ resistor and the voltage across this resistor is recorded by an oscilloscope. The Tektronix P6015A voltage monitor has 100 MΩ resistor (and a very small inductance which is neglected) and its voltage is recorded similarly. The Pearson CVT 411 current monitor is represented by the total current flowing in the mesh.

This empirically derived equivalent circuit model is based upon parameter fits to several open and short circuit calibration tests. None of the electrical characteristics of any of the components have been explicitly measured.

DISCUSSION OF EXPERIMENTAL AND SIMULATION RESULTS

A detailed investigation of certain features of wire burst was undertaken. These features include wires bursting in air at their ends near the electrodes; and wires bursting when confined by a potted material.

An Investigation of Wire Burst in Air

The experiments and computational analyses show that a wire burst initiates near the upper and lower electrodes [4]. Figure 7 shows the early time development of this phenomenon, however, the mechanism for this phenomenon has not been previously explained. Wire initiation near the electrodes and hemispherical shock formation is

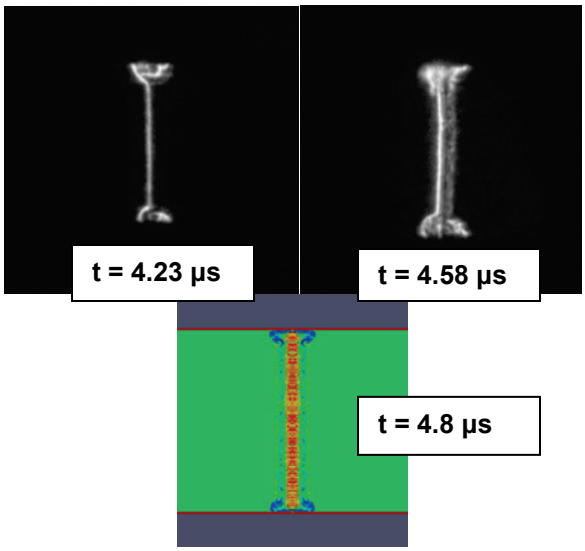

Figure 7. Two experimental ANDOR ICCD CAMERA images and one simulation image of wire burst showing the burst and shock waves emanate from the ends of the 10 mm long aluminum wire near the electrodes.

seen in experiments at 10, 5, and 3 mm gaps. At 1 mm gaps and smaller, initiation at the wire ends is difficult to image or else the ANDOR ICCD camera is not used. Simulations show that initiation near the ends of the wires persists down to 0.3 mm gaps and the two shocks merge immediately. Below this separation individual shocks cannot form because the ends are too close. Since the mechanism for burst near the electrodes persists down to such small electrode separation, it is conjectured that this mechanism remains important. For instance, wire burst for very small inter-electrode gaps may burst sooner than longer wires due to this effect, especially near mid gap. This section investigates the details of wire burst close to the electrodes.

Wire initiation has long been a topic of interest in the study of wire array Z pinches by researchers at the national laboratories and numerous universities [5-14,20]. Most of these studies show the wire exploding along its entire length. End effects may be present, however they are of a different nature than the effects seen here. No case found in the cited and related references shows wire burst and shock formation at the ends of the wires, therefore fast Z pinch research is of limited value in understanding the phenomenon seen here, and there are several reasons why this is so. Wire array Z pinches are initiated under vacuum, and not in air. Wires in a Z pinch load are on the order of 10 microns in diameter, whereas the majority of the wires in these experiments are on the order of 96 microns in

diameter. The rise time of the Z pinch current pulse is shorter, being on the order of 120 to 200 ns, as opposed to the 1.5 μs rise time for lightning-like pulses. Also, a 20 MA Z pinch driver with a 300 wire array has 66 MA per wire, whereas here there is only 1 to 3 MA per wire.

Initiation of wire burst when the wire is submerged in deionized water is also seen to originate near the electrodes (see Figure 8). The burst of 10 mm long, 96 micron diameter wires from Shots 41, 42 and 44 (only Shot 44 is shown) show evidence of burst and shock formation originating near the electrodes. Earlier reports found in the literature of microsecond time-scale, explosion of metal wires in water (and glass capillaries) are of similar time scales and current levels as the experiments conducted in this project. The wires are copper, aluminum or tungsten, of larger 125 to 250 micron diameter, and of longer 22 mm length or more [15-19]. These articles are primarily concerned with the measurement of the electrical conductivity and the expanding diameter of the wire is imaged only at the wire's midplane. No mention is made of end effects. If end effects did occur, there would be insufficient time for the shock waves to reach the midplane and be imaged because of the long length of the wires. Therefore, it is unknown whether the phenomenon of wire burst initiating near the electrodes has manifested itself before or if it something unique to these experiments.

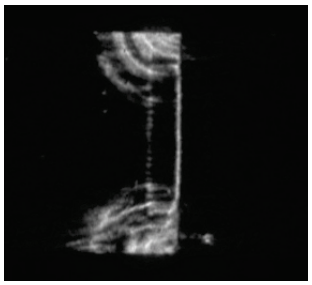

Figure 8. Burst of 10 mm long wire in water from Shot 44 show evidence of burst and shock formation beginning near the electrodes.

In order to explore the detailed physics of the initial wire burst, we model Shot 7. This shot used a 5 mm long, 96.4 micron diameter aluminum wire between two 1 inch diameter aluminum electrodes. The current and voltage pulses for Shot 7 are shown in Figure 9. The experimental data is time shifted so that the arrival of the current pulse defines starting point of the simulations. The simulations are run according to the setup shown in Figure 3, and are driven using the measured current profile shown in Figure 9.

In the course of the simulation, very little current transfers from the wire material to the surrounding air. The magnitude of the magnetic field ranges from 0 to 4 T. The peak magnetic field is nominally 4 T, based upon a nearly 2 kA peak current and 100 micron radius. The peak magnetic pressure associated with this field is only about 6.4 MPa, which is insufficient to confine the approximately 1 GPa pressures generated in the wire at the time of burst.

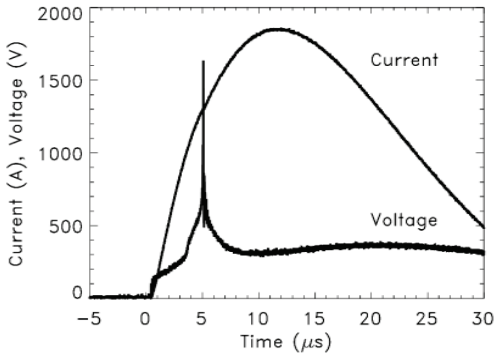

Figure 9. Load current and voltage profiles for Shot 7.

Figure 10 plots four snapshots of magnified images of the wire near the upper electrode showing the temperature and density state of the wire. Lines are superimposed on each plot to denote the original radius of the wire and the surface of the electrode. Each snapshot compares the temperature on the left and the density on the right. The range of the temperature scale changes in the 4 frames due to the increase in the temperature up to about 3000 K. The range of the density scale is logarithmic and remains fixed and covers 4 orders of magnitude from 0.1 kg/m^3 up to solid density of 2700 kg/m^3. Superimposed upon the plots are the current density streamlines (contours of constant $\psi = r \bullet B_\theta$) colored by the magnetic field strength.

In the top frame of Figure 10 when the temperature of the wire material is below melt of ~933 ^{o}K, the current streamlines are uniform throughout the wire except near the ends where the transition to the electrode pulls the current to a larger radius. The Joule energy deposition preferentially heats the outer corner of the wire due to the non-uniform distribution of the current density, and is consistent with the theory and analysis of the contact

resistance between conductors of different radii or of dissimilar materials [20-23]. In this regime, the electrical resistivity increases and the thermal conductivity decreases in the solid wire linearly with temperature increase. The electrodes also appear to serve as heat sinks over these time scales as evidenced by the temperature gradients. The outward heat transfer is into the large mass of the electrode keeping the end of the wire abutted to the electrode cooler. The inward heat transfer initially heats the wire mass at height equal to 1 to 2 wire radii from the electrode. This seed the subsequent evolution of the wire.

In the second frame of Figure 10, the wire temperature now exceeds melt and nearly uniform radial expansion of the wire begins as the wire pressure exceeds both the confining magnetic field pressure and the surrounding air pressure. However, a small amount of necking is apparent at a height that is approximately 1 wire diameter from the electrode. The cause may be a slightly larger magnetic field due to the sum of the axially flowing current in the wire and the radially flowing current in the electrode. Also, a slightly elevated temperature is evident in the neck region due to the slightly higher current density. The thermal and electrical conductivities continue to drop as the temperature increases and the density begins to drop.

The wire material closest to the electrode now expands the most due the previous corner hot spot. A new hot spot begins to form in the neck region due to a combination of the high current density concentration and slightly lower electrical conductivity (higher resistivity). The thermal conductivity is also lowest in the neck region, implying that Joule energy deposited in this region is slower to be conducted away. This provides a feedback mechanism to enhance the heating in this region, as well as the seed for the subsequent explosion.

In the bottom two frames of Figure 10, the temperature continues to rise and the conductivities continue to drop in the neck region, more so than in the bulk of the wire. Joule energy deposition remains greatest in this region due to the higher resistivity, and the heat is not conducted away due to the lower thermal conductivity. The elevated temperature eventually causes the pressure in the neck region to exceed that of the bulk of the wire. The higher pressure then causes this region to expand faster than the bulk of the wire; hence the neck has expanded to match the radius of the bulk of the wire.

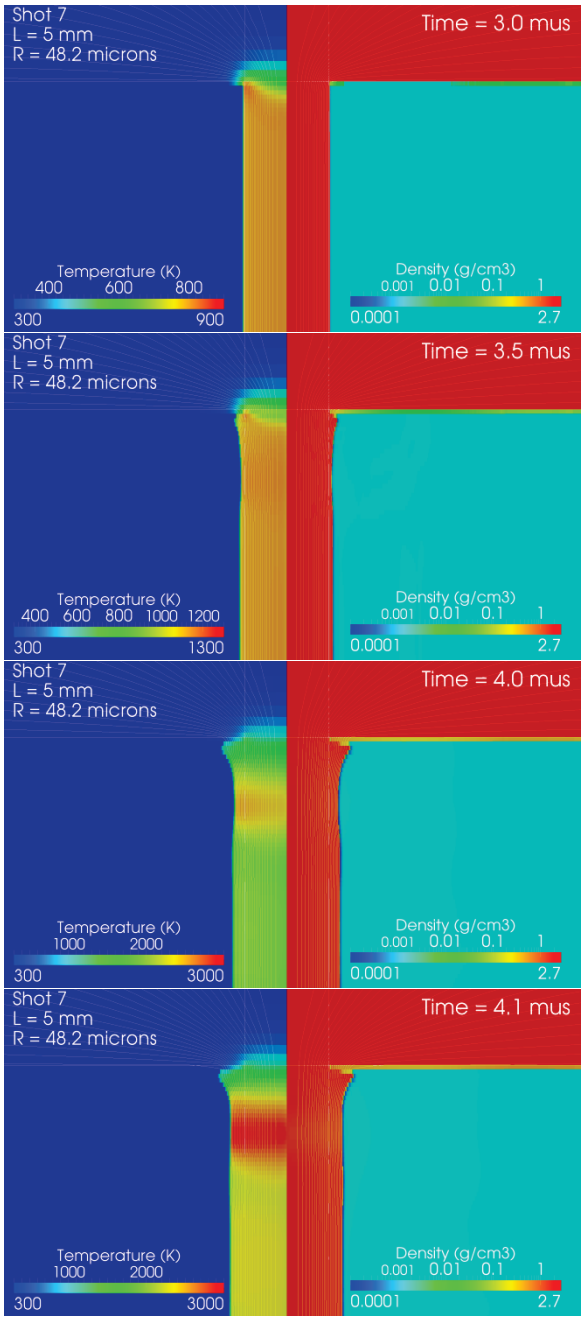

Figure 10. Simulation of Shot 7 of wire burst in air at 3.0, 3.5, 4.0 and 4.1 μs afer pulse arrival. Currents are 966, 1085, 1198, and 1212 A, respectively.

In Figure 11, we add plots of the thermal conductivity on the bottom left and the electrical conductivity on the bottom right. The thermal conductivity color scale is linear and fixed and ranges from 0 to 200 J/m/s/K. The electrical conductivity color scale is fixed and logarithmic and covers 8 orders of magnitude from 10^{-1} to 10^{7} S/m

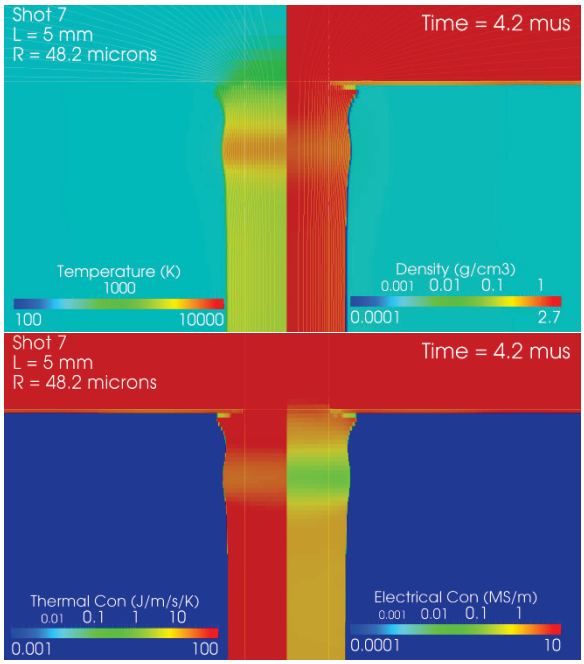

Figure 11. Simulation of Shot 7 of wire burst in air at 4.2 μs afer pulse arrival. Current is 1233 A.

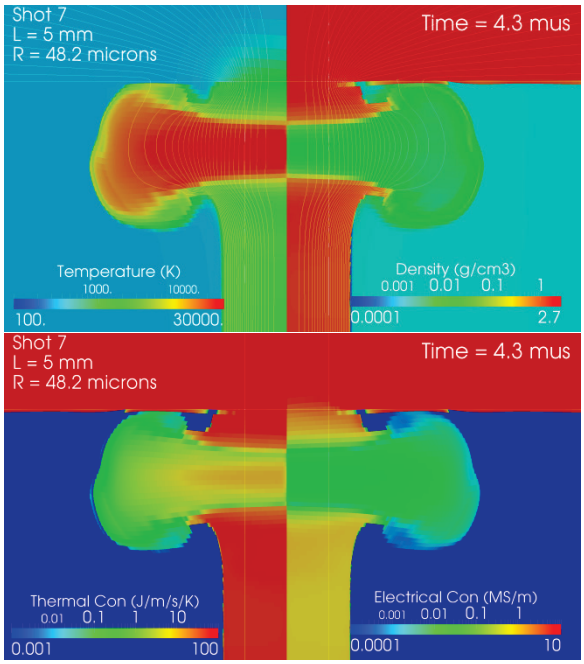

Figure 12. Simulation of Shot 7 of wire burst in air at 4.3 μs afer pulse arrival. Current is 1256 A.

(Siemens/m). The value 10^{-1} S/m is the lower electrical conductivity limit chosen for use in the magnetic field solver and is also used as the limiting value for insulating materials even though the real conductivity may be lower.

In Figure 11, the region that was once a neck now becomes a bulge. Wire explosion is imminent. Material in this region is vaporizing and partially ionizing. The thermal conductivity in the bulge has dropped sufficiently that the bulk of the wire is now thermally isolated from the electrodes. The electrical conductivity drop (resistivity rise) is responsible for the resistive voltage spike seen in the electrical measurements. The small expansion of the wire and the relatively constant rate of current change means that the inductive component of voltage spike is smaller than the resistive component. When the wire bursts the solid aluminum wire vaporizes and ionizes and the density drops to a level that is on the order of the surrounding air density of 1.218 kg/m^3.

In Figure 12, hot plasma explosion begins when the wire material reaches the top of the vapor dome in pressure-density-temperature EOS phase space. The wire bursts in a region that is at a height that is nominally between 1 wire radius and 1 wire diameter from the electrode as seeded by the earlier evolution of the material in this region. The magnetic field is largely frozen into and expands with the plasma. The bulk of the wire between the electrodes is thermally isolated from the electrodes. Subsequent Joule heating of the remainder of the wire eventually results in a cylindrical explosion of that portion of the wire.

Seeing as how the region of initial wire burst appears to lie at an axial height that is between 1 wire radius and 1 wire diameter, it was speculated that geometry and thermal conduction plays a role. Temperature gradients in the radial direction are limited by the wire radius, so this might cause a similar limitation in the axial direction near the end of the wire. Also, few microseconds time scale is sufficient time for significant thermal conduction to occur from the wire end into either the electrode or toward the central portion of the wire. Therefore a direct comparison of two simulations with and without thermal conduction was performed. It was found that the same basic phenomenology is present whether thermal conduction is arbitrarily turned on or off. The main difference is that wires burst about 70 ns later when there is no thermal conduction compared to simulations with thermal conduction. Therefore, thermal conduction of heat is not a cause of wire burst near the electrodes, leaving us to conclude that the best explanation is the enhanced Joule heating caused by the concentration of the current as it transitions from the wire to the electrode.

Even though the wire diameters, current levels and time scales in these experiments are different than

those of Z pinch wire initiation experiments, the region of equation of state (EOS) and electrical conductivity traversed is similar. Ref. 11 shows phase space plots of the material state as the wire transitions to an exploded state. Similar plots describe the explosion process outlined here with the explosion region near the ends of the wire near the electrodes advancing over the vapor dome first. In some respects the simulation presented here should have greater fidelity to the experiments than simulations in vacuum because the surrounding air tamps the wire expansion and potentially unphysical ultra-low density material is excluded from the present simulations.

Simulation of Wire Bursts Confined by Alternate Materials

With an understanding of wire burst in air, we now briefly consider wire burst in denser and also some opaque materials such as water, epoxy, and PMMA (Plexiglas). Since these alternate materials are non-conducting, we expect that the mechanism of wire burst near the electrodes to still be valid, even though any expansion will be strongly tamped. All of the simulations in this section are driven using the complete circuit model described previously. The four materials provide different levels of radial confinement. The choice of materials is dictated by the materials with equation of state (EOS) and conductivity models available.

Figure 13 compares the current and voltage signals among these 4 materials. The wire voltage produced when confined by water spikes is similar to the voltage produced when the wire is confined by air. This is because the ablated wire material can still expand in a manner similar to what has already been seen in air. Therefore the electrical and thermal conductivity also drops in a similar manner leading to the voltage spike.

By contrast, the simulation of wire burst confined by PMMA does not exhibit a high voltage spike. Instead the wire material is confined by the PMMA preventing the low density expansion, and hence the low conductivity (high resistivity) region which is the cause of the voltage spike.

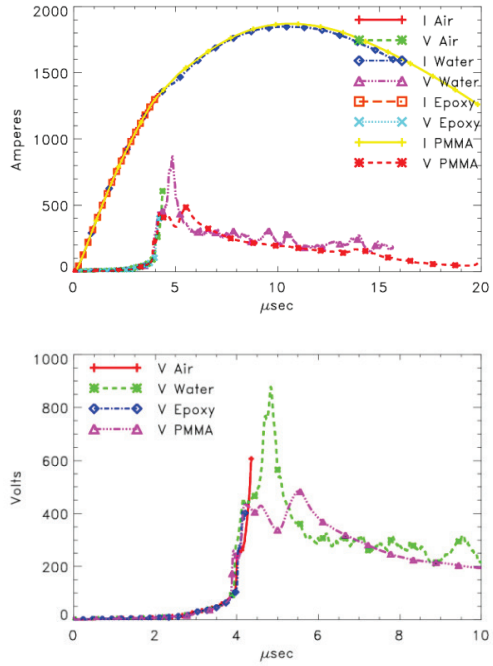

Figure 13. Comparison of current (top) and voltage (bottom) profiles from simulations of 2-mm long wire burst confined by air, water, epoxy, and PMMA and driven by the same circuit model. While the current profiles through the wires confined by the different materials are similar, the voltage profiles differ significantly depending on the expansion of wire material near the electrodes.

Figure 14 compares the spatial pressure profiles produced in water and in PMMA at two times in the burst process. In water the wire material can expand limiting the pressure build-up in the wire. The impulse drives a relatively slower hemispherical shock determined by the properties of water that stays below 1 GPa. In contrast the PMMA strongly limits expansion of the wire material keeping the Joule heating and pressure build up confined to a smaller volume. The impulse drives a stronger faster shock greater than 1 GPa into the PMMA that is governed by the properties of the PMMA. The bottom frame of Figure 14 shows consolidation of upper and lower shocks long before the consolidation in water.

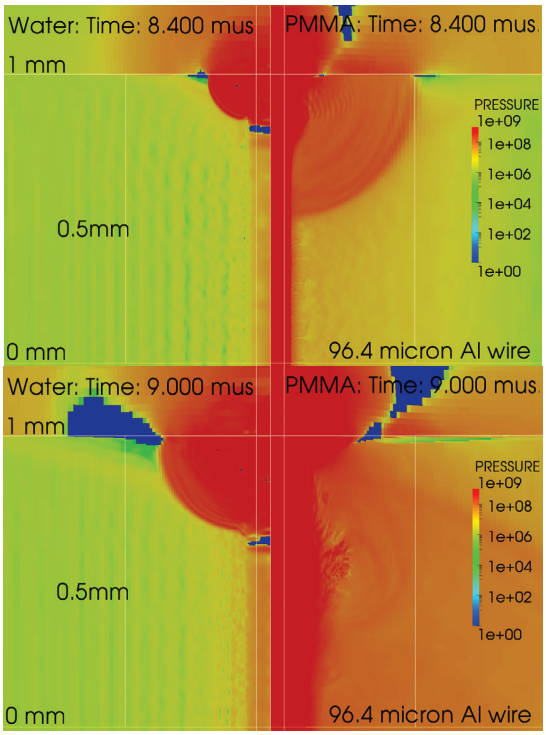

Figure 14. Comparison of 2-mm long wire burst confined by water (left) and PMMA (right) at the time of wire burst (8.4 μs) and shortly thereafter (9.0 μs).

Comparison to experiments of wire burst in water

Water is nominally 1000 times denser than air, but has no strength. Water tamps the expansion of vaporized wire material more than air, but wire initiation still begins near the upper and lower electrodes as previously seen in the Schlieren photograph of Figure 8, as well as in the simulation shown in the left hand side of Figure 14. The strongest intensity shock expands hemispherically from wire/electrode interfaces. Weak shocks and oscillations also emanate from the bulk of the wire into surrounding water.

Comparison to experiments of wire burst in epoxy

Six shots of a 96.4-μm wire radially confined by epoxy were conducted. Wire lengths varied between 0.84 mm and 2.02 mm. The pulse generator voltage was set at 1 kV and the current to 1.6 kA peak. The epoxy was Epon838 with 30% Jeffamine as a curing agent.

The epoxy experiments exhibited both single and double, and even triple, voltage spikes. An example of a single voltage spike is shown in Figure 15. The double pulse voltage spikes are not very different than the double spike shown in Figure 17 for PMMA. There is no strong correlation between the number of voltage spikes with epoxy and gap thickness. There is significant shot-to-shot variation. Such variation needs to be eliminated if epoxy is to be used to validate code results.

Unfortunately only incomplete simulation data is available due to exceedingly small time steps at the time of the voltage spike, hence the whole voltage spike has yet to be computed in an epoxy simulation. However, as can be seen from Figure 13, the early time history of the simulated voltage and current pulse are consistent with the profiles for the other materials.

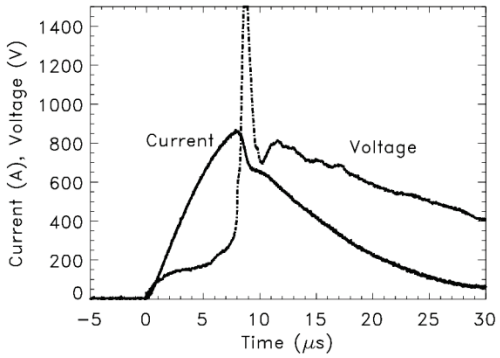

Figure 15. One example of experimental voltage and current profiles for wire burst of a 2.02-mm aluminum wire radially confined by epoxy from Shot 122.

Comparison to experiments of wire burst in PMMA

Ten shots of a 96.4-μm wire radially confined by PMMA were conducted. Wire lengths varied between nominally 0.77 mm and 1.60 mm. The pulse generator voltage was set at 1 kV and the current to 1.6 kA peak.

The PMMA experiments also exhibited both single and double voltage spikes. An example of a single voltage spike is shown in Figure 16 and a double voltage spikes is shown in Figure 17. Single voltage spikes are mostly correlated with 1 mm PMMA thicknesses and inter-electrode gaps, while double voltage spikes are mostly correlated with 2 mm PMMA thicknesses and inter-electrode gaps, although there are exceptions. Like epoxy, such variation needs to be eliminated if PMMA is to be used to validate code results.

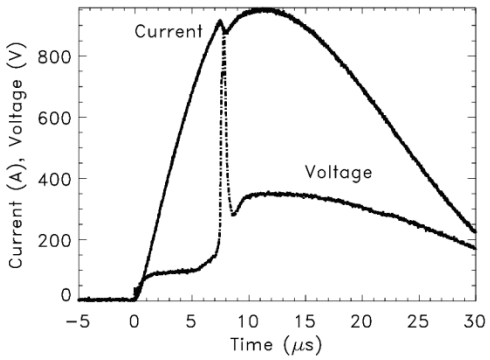

Figure 16. One example of experimental voltage and current profiles for wire burst of a 1-mm aluminum wire radially confined by PMMA from Shot 129.

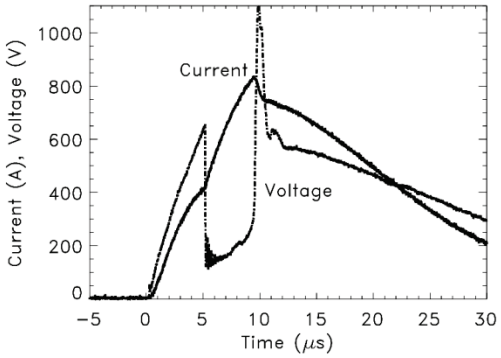

Figure 17. One example of experimental voltage and current profiles for wire burst of a 1.53-mm aluminum wire radially confined by PMMA from Shot 131.

CONCLUSIONS

We have presented the results of experiments and simulations that quantify the behavior of confined arcs as modeled by short aluminum wires embedded in materials confined between two flat electrodes. To the extent possible, the experiments have been used to validate many aspects of the simulations. Discrepancies point to areas where improvements are needed.

ACKNOWLEDGMENTS

This work is sponsored by the Boeing Company through a Cooperative Research and Development Agreement with Sandia National Laboratories under contract PTS No. 1651.15.05. Sandia National Laboratories is a multi-program laboratory managed and operated by Sandia Corporation, a wholly owned subsidiary of Lockheed Martin Company, for the U. S. Department of Energy's National Nuclear Security Administration under contract DE-AC04-94AL85000.

REFERENCES

1. A.C. Robinson, et al. ALEGRA: An Arbitrary Lagrangian-Eulerian Multimaterial, Multiphysics Code, Proceedings of the 46th AIAA Aerospace Sciences Meeting, Reno, NV; AIAA Paper, 2008–1235, (2008).
2. A.C. Robinson, J.H.J. Niederhaus, V.G. Weirs and E. Love, Arbitrary Lagrangian-Eulerian 3D ideal MHD algorithms, Int. J. Numer. Meth. Fluids, 65, 1438–1450, (2011).
3. W.J. Rider, E. Love, M.K. Wong, O.E. Strack, S.V. Petney, and D.A. Labreche, Adaptive methods for multi-material ALE hydrodynamics, Int. J. Numer. Meth. Fluids, 65, 1325–1337, (2011).
4. J.M. Lehr, Z.R. Wallace, M. Caldwell, A.C. Day, S. Chantrenne, and K.C. Hodge, Wire Burst Experiments and Modeling Phase II: Confined Geometries, Technical Report SAND2012-8698, Sandia National Laboratories, Albuquerque, NM, October 2012.
5. D.H. Kalantar and D.A. Hammer, Observation of a Stable Dense Core within an Unstable Coronal Plasma in Wire-Initiated Dense Z-Pinch Experiments, Phys. Rev. Lett., 71 (23) 3806, (1993).
6. F.N. Beg, A.E. Dangor, P. Lee, M. Tatarakis, S.L. Niffikeer, and M.G. Haines, Optical and x-ray observations of carbon and aluminum fibre Z-pinch plasmas, Plasma Phys. Control. Fusion, 39, 1-25, (1997).
7. J. Ruiz-Camacho, F.N. Beg, A.E. Dangor, M.G. Haines, E.L. Clark, and I. Ross, Z-pinch discharges in aluminum and tungsten wires, Phys. Plasmas, 6 (6) 2579, (1999).
8. D.B. Sinars, T.A. Shelkovenko, S.A. Pikuz, M. Hu, V.M. Romanova, K.M. Chandler, J.B. Greenly, D.A. Hammer, and B.R. Kusse, Effect on insulating coatings on exploding wire formation, Phys. Plasmas, 7 (2) 429, (2000).
9. D.B. Sinars, M. Hu, K.M. Chandler, T.A. Shelkovenko, S.A. Pikuz, J.B. Greenly, D.A. Hammer, and B.R. Kusse, Experiments measuring the initial energy deposition, expansion rates and morphology of exploding wires with about 1 kA/wire, Phys. Plasmas, 8 (1) 216, (2001).
10. D.A. Hammer and D.B. Sinars, Single-wire explosion experiments relevant to the initial

stages of wire array Z pinches, Laser Part. Beams, 19, 377-391, (2001).
11. G.S. Sarkisov, S.E. Rosenthal, K.R. Cochrane, K.W. Struve, C. Deeney, and D.H. McDaniel, Nanosecond electrical explosion of thin aluminum wires in a vacuum: Experimental and computational investigations, Phys. Rev. E, 71, 046404 (2005).
12. G.S. Sarkisov, K.W. Struve, and D.H. McDaniel, Effect of deposited energy on the structure of an exploding tungsten wire core in a vacuum, Phys. Plasmas, 12, 052702, (2005).
13. T.J. Awe, B.S. Bauer, S. Fuelling, and R.E. Siemon, Threshold for Thermal Ionization of an Aluminum Surface by Pulsed Megagauss Magnetic Field, Phys. Rev. Lett., 104, 035001 (2010).
14. T.J. Awe, B.S. Bauer, S. Fuelling, I.R. Lindemuth, and R.E. Siemon, Experimental investigation of thermal plasma formation from thick aluminum surfaces by pulsed multimegagauss magnetic field, Phys. Plasmas, 17, 102507 (2010).
15. A.W. DeSilva, H.J. Kunze, Experimental study of the electrica conductivity of strongly coupled copper plasma, Phys. Rev. E, 49 (5) 4448, (1994).
16. N.I. Kuskova, S.I. Tkachenko, and S.V. Koval, Investigation of liquid metallic wire heating dynamics, J. Phys.: Condens. Matter, 9, 6175-6184, (1997).
17. A.W. DeSilva and J.D. Katsouros, Electrical conductivity of dense copper and aluminum plasmas, Phys. Rev. E, 57 (5) 5945, (1998).
18. A.W. DeSilva and J.D. Katsouros, Measurement of the Electrical Conductivity of Metals in the Vicinity of the Critical Point, Int. J. Thermophys., 20 (4) 1267, (1999).
19. A.W. DeSilva and A.D. Rakhel, Electrical Resistivity and Thermodynamic Properties of Dense Tungsten Plasma, Int. J. Thermophys., 26 (4) 1137, (2005).
20. M.R. Gomez, J.C. Zeir, R.M. Gilgenbach, D.M. French, W. Tang, and Y.Y. Lau, Effect of soft metal gasket contacts on contact resistance, energy deposition, and plasma expansion profile in a wire array Z pinch, Rev. Sci. Instrum., 79, 093512 (2008).
21. P. Zhang and Y.Y. Lau, Scaling laws for electrical contact resistance with dissimilar materials, J. Appl. Phys., 108, 044914 (2010).
22. P. Zhang, Y.Y. Lau, and R.M. Gilgenbach, Minimization of thin film contact resistance, Appl. Phys. Lett., 97, 204103 (2010).
23. P. Zhang and Y.Y. Lau, Thin film contact resistance with dissimilar materials, J. Appl. Phys., 109, 124910 (2011).